IEEE Access
Multidisciplinary | Rapid Review | Open Access Journal

Received March 5, 2020, accepted March 21, 2020, date of publication March 26, 2020, date of current version April 15, 2020.

Digital Object Identifier 10.1109/ACCESS.2020.2983591

Electrochemical Dissolution Behavior of Nickel-Based Hastelloy X Superalloy at Low Current Densities

YINGYUE YIN[1,2,3], JIANHUA ZHANG[1,2,3], YUCAI MA[1,2,3], JINXING HUO[1,2,3], KAI ZHAO[4], XIANGYU MENG[1,2,3], QUANQUAN HAN[1,2,3], AND JICAI YIN[5]

[1]School of Mechanical Engineering, Shandong University, Jinan 250061, China
[2]Key Laboratory of High Efficiency and Clean Mechanical Manufacture, Ministry of Education of China, Jinan 250061, China
[3]National Demonstration Center for Experimental Mechanical Engineering Education, Jinan 250061, China
[4]Key Laboratory for Liquid-Solid Structural Evolution and Processing of Materials, Ministry of Education, Shandong University, Jinan 250061, China
[5]School of Mechanical and Architectural Engineering, Taishan University, Tai'an 271000, China

Corresponding authors: Jianhua Zhang (jhzhang@sdu.edu.cn) and Quanquan Han (hanquanquan@sdu.edu.cn)

This work was supported in part by the National Key Research and Development Plan under Grant 2018YFB1105903, and in part by the Science and Technology Development Project of Tai'an under Grant 2017GX0021.

ABSTRACT Electrochemical machining (ECM) is a proven processing technique for fabricating difficult-to-cut nickel-based superalloys with complex shapes using the principle of anodic dissolution. However, the metallic surface is susceptible to stray corrosion under conditions of low current density, which increases the difficulty of using ECM on nickel-based superalloy such as Hastelloy X (HX). In this study the electrochemical dissolution behavior of wrought HX at low current density was systematically analyzed. The results revealed that $M_{23}C_6$ carbides were irregularly distributed on the grain boundaries. The polarization curves and open-circuit potential measurements showed that an appropriate temperature (35°C) and concentration (10 wt.%) aided in the formation of efficient and stable dissolution in $NaNO_3$ solution. The findings also revealed that selective corrosion occurred preferentially on the grain boundary or near the $M_{23}C_6$ precipitations after passivation film polarization. After careful investigation of the different-stage dissolution microstructures and the solid black block-shape products, $M_{23}C_6$ precipitation was found to play a key role in the dissolution of HX alloy at low current density. A qualitative model was established to demonstrate the electrochemical dissolution behavior of wrought HX alloy in $NaNO_3$ solution. This model offers a new insight into the suppression of stray corrosion of Ni-based superalloys in aerospace applications.

INDEX TERMS Hastelloy X, microstructure, electrochemical dissolution behavior, selective corrosion.

I. INTRODUCTION

Electrochemical machining (ECM) is an advanced technology for shaping difficult-to-machine materials. It employs the dissolution of anodic metals and thereby bypasses the limitations of the alloy's mechanical properties [1], [2]. Compared to conventional machining techniques, ECM offers several advantages, such as high metal removal rate, reduced tool wear, lower residual stress, and excellent ability to cast complex shapes [3]–[5]. ECM has garnered considerable attention in the past decades due to its potential applications in electrochemical micromachining of silicon [6] or gallium nitride [7], [8] as well as other applications such as MEMS [9], sensors, photonics [10], or superalloy fabrication.

The associate editor coordinating the review of this manuscript and approving it for publication was Dinesh Thanu.

Over the years, various ECM processes of nickel-based alloys were primarily focused on machining at high current density (20–200 A/cm^2) [11]. In many operating conditions, however, the machining area of the workpiece is subjected to a low-current-density electric field (generally less than 5 A/cm^2); this could cause further uneven electrochemical corrosion, a defect known in electrochemical processing as the stray corrosion phenomenon [12], [13]. Also, the machining accuracy and surface quality of the workpiece is significantly degraded.

ECM is primarily influenced by certain key factors, such as physical properties of the workpiece, electrolyte [14]–[16], and power supply [17], [18]. Over the past few years, several studies have focused on the influence of electrolyte and power supply on the surface integrity of processing. For instance, Wang *et al.* studied the influence of electrolyte

flow rate on the machining accuracy of Inconel 718 can contribute to the formation of uniform contour of the hole [19]. Fang *et al.* [20] studied the effect of pulsating electrolyte flow on the electrochemical machining efficiency of Inconel 718, and they found that the employment of appropriate pulsation parameters enhanced the material removal rate. Furthermore, the increase in pulse frequency and decrease in pulse width favored an enhancement in surface quality [21].

The anodic dissolution behavior of metals is significantly affected by the microstructure feathers. Some reports have shown that AZ31 Mg alloy and Ti-6Al-4V within a large amount of acicular α' martensite can easily cause anodic dissolution under low current densities [22], [23]. For instance, Dai *et al*. compared the corrosion resistance of Ti-6Al-4V alloy prepared by selective laser melting (SLM) with commercial grade 5 alloys in NaCl solution; they found that the SLM fabricated Ti-6Al-4V alloy showed a lower corrosion resistance due to the microstructure produced by SLM with a small amount of ß-Ti phase and more α'-Ti phase [24]. In addition, a large number of grain boundaries and grain planes with a higher surface energy contribute to higher electrochemical dissolution rates [25], [26]. Guo *et al*. [27], [28] investigated the electrochemical anodic behaviors that occur due to the phase constituent and crystallographic texture of Inconel 718; The authors found that the γ matrix around the Nb-rich γ phase preferentially dissolved. Also, the columnar structure contributed to the electrochemical anode dissolution anisotropy.

In general, anodic dissolution behavior is a part of the guiding theories in ECM, whereas stray corrosion at low current densities affects the machining accuracy during the ECM process. However, few studies have considered the anodic dissolution of wrought nickel-based alloys under low current densities. Therefore, it is necessary to systematically investigate the correlation between microstructure and dissolution behavior at low current density, which may offer theoretical guidance to avoid stray corrosion in ECM process.

II. EXPERIMENTAL PROCEDURES

A. MATERIAL

Due to its great tensile strength and unique advantages in resisting oxidation, corrosion, and high temperature fatigue, Hastelloy X (HX) has been widely used in the fabrication of key engineering components such as gas turbine combustors, transition parts, and exhaust end components [29], [30]. The wrought HX alloy used in this study has a chemical composition (wt.%) of Cr 21.7- Fe 19.3-Mo 9.1-Co 1.3-W 0.46-Si 0.71-C 0.09-Cu 0.26-N 0.01-P 0.025-bal. Ni. The plate was a solution annealed at 1150 °C for 30 minutes, followed by water cooling. The cylindrical workpieces with a diameter of 14.8 mm and height of 2 mm were then cut from this plate using wire-electrode cutting for metallographic examination and electrochemical polarization tests. Prior to the experiments, all the workpieces were manually grinded successively by SiC papers (from #120 to 2000), and then mechanically polished with diamond abrasive particles with particle size of 0.5 μm and 0.25 μm. Finally, the wrought HX was washed with anhydrous ethanol and dried with flowing air.

B. MATERIAL CHARACTERIZATION

The microstructure of the HX alloy was characterized using scanning electron microscopy (SEM; JEOL, JSM-7800F) equipped with an electron backscatter diffraction (electron backscattered scattering detection (EBSD) system, Oxford Nordlys Max3). To reveal the HX microstructure, the workpiece was chemically etched with a mixed solution (2 g of $CuCl_2$, 40 ml of HCl, and 80 ml of anhydrous ethanol) for about 35 s. The chemical composition analysis was performed by an X-ray energy dispersive spectrum (EDS) with an acceleration voltage of 15 kV. The micro-area analysis of elemental distribution was conducted with an electron probe micro-analyzer (JEOL, EPMA-JXA-8530F plus). The transmission electron microscope (TEM) samples were ground to ~100-μm thickness, and a hole of 3-mm diameter was punched. The further analysis of corrosion products of HX were performed (hv = 1486.6 eV, 300 W) at 50 kV and 150 mA in the X-ray photoelectron spectroscopy (XPS) system. The C1s (285.0 eV) standard peak was used to regulate the XPS spectrum before analyzing the fitting data. The CasaXPS software was used to analyze the corrected data after subtracting the baseline.

C. ELECTROCHEMICAL TESTING

The polarization curve measurements were performed using a CS310H electrochemical workstation and a typical three electrode cell, which consisted of a saturated calomel electrode (SCE), a platinum counter electrode, and a cylindrical working electrode. $NaNO_3$ and NaCl solution was used as the electrolyte, and the surface air oxide film was removed by polarization for 2 min at a constant potential of −1.2 V. The scanning rate using in the polarization tests was 1 mV/s, and the potential was then set from −1.5 V to 2.7 V (vs. the SCE). The electrochemical tests were conducted 3 times for each sample to ensure consistency.

III. RESULTS AND DISCUSSION

A. MICROSTRUCTURE CHARACTERISTICS

Microstructure characterization of wrought HX cross sections after solution annealing revealed the typical grain morphology in Fig. 1. The HX alloy was found to contain a great deal of equiaxed grains with a size of 30-50 μm. In addition to the observed equiaxed grains, some gray block-shaped precipitates were also observed in the magnified image. Micron-sized, gray block-shaped particles are discontinuously distributed along grain boundaries, while there are a number of dispersed particles observed within the grains. This is consistent with the results reported in previous studies by Kinzel *et al.*, which were obtained by scanning

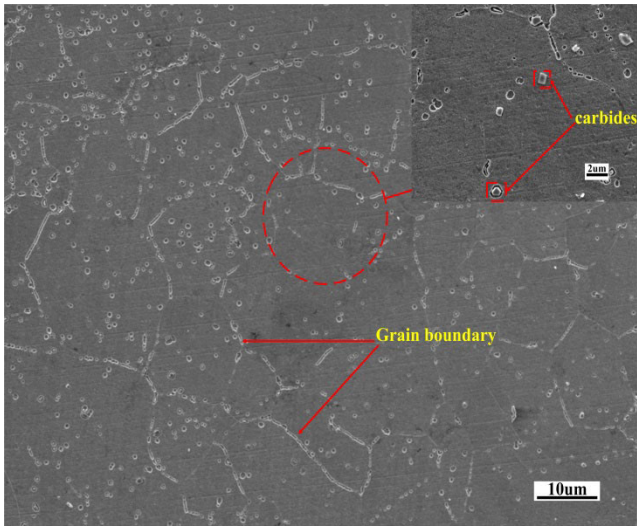

FIGURE 1. SEM images of microstructure from wrought HX cross sections after solution annealing.

electron microscopy (SEM) and atom probe tomography (APT) [31]–[33].

Fig. 2 shows the electron probe micro analyzer (EPMA) images of the HX alloy; these images are useful for understanding the precipitation of elements in HX. Based on the back-scattered electron (BSE) image of the carbides (Fig. 2a), a large number of small precipitated particles are observed and distributed on the grain boundaries. The distribution of Ni, Cr, Mo, and C is shown in Figs. 2b–e, respectively. The results reveal that the particles in the grain and on the grain boundaries contain Cr-enriched, Mo-enriched, and C-enriched elements. The surface of the gray particles was lacking Ni. This could be explained by the fact that the enrichment of Cr on the edge of the dendrites promoted the formation of Cr-rich carbides during HX solidification.

Fig. 3 shows the bright-field TEM images from the HX alloy used in the present study. These images are useful for further investigation of the microstructure and precipitation in HX. The black block-shape precipitation (marked by the red circle in Fig. 3a) is carbide with the general formula of $M_{23}C_6$ as further verified by selected area diffraction pattern (SADP), as shown in Fig. 3b. The results suggest that this carbide has a face-centered cubic (FCC) crystal structure with a lattice parameter of 10.767 Å. In addition to the diffraction spots from $M_{23}C_6$, diffraction spots from a γ matrix phase (marked by the red rectangle) in Fig. 3a with an FCC structure are also verified by SADP in Fig. 3c. Compared to the marked area 2, area 1 was found to exhibit a stronger element precipitation, and this can be confirmed by the chemical composition analysis (Table 1). Area 1 also revealed that $M_{23}C_6$ precipitates with a block-shape appearing as black in the bright-field TEM were Ni deficient. This is consistent with the results of the element distribution of gray carbide particles in Fig. 2. One possible explanation is that between the $M_{23}C_6$ and γ matrix, a significant compositional segregation exists during HX solidification. This was similar to the findings of Marchese *et al.* [34], [35], which found that carbides rich in Mo formed in the as-built state.

Hence, it may be concluded that the precipitates on the grain boundaries and within the grains were $M_{23}C_6$ type carbides, which formed because of compositional segregation during HX solidification.

B. ELECTROCHEMICAL DISSOLUTION BEHAVIOR

The electrolyte type, concentration, and temperature are considered to be significant to obtain a stable and efficient dissolution in the electrochemical dissolution process. Aqueous $NaNO_3$ and NaCl solutions were two neutral electrolytes that are widely used to investigate the electrochemical dissolution behavior and were therefore selected for this study. Prior to the polarization tests, relatively stable open circuit potentials (OCPs) of each workpiece were measured in the NaCl and $NaNO_3$ solutions, respectively. Apart from the 10 wt.% $NaNO_3$ solution, the OCPs in other solutions exhibited a similar tendency in which E_{ocp} decreased with immersion time, as shown in Fig. 4. However, the E_{ocp} in 10 wt.% $NaNO_3$ solution was found to increase with immersion time

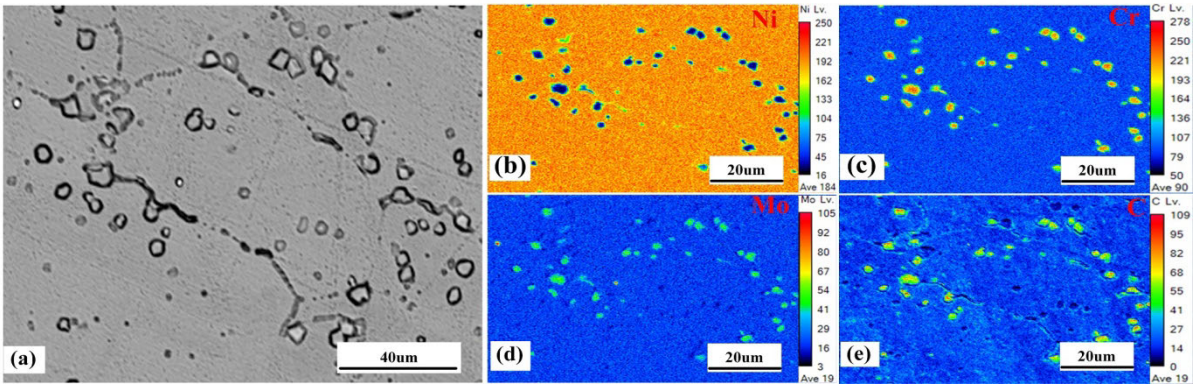

FIGURE 2. EPMA images of carbides on wrought HX. (a) BSE morphology of carbides on the boundary or in the grain; distribution element of (b) Ni; (c) Cr; (d) Mo; (e) C.

TABLE 1. Chemical COMPOSITIONS OF THE DIFFERENT POSITION (atomic percentage %)

Position	C(K)	Cr(K)	W(K)	Fe(K)	Ni(K)	Mo(K)
1	9.01	57.09	0.19	9.00	20.04	4.64
2	1.74	22.33	0.19	20.91	51.96	2.57

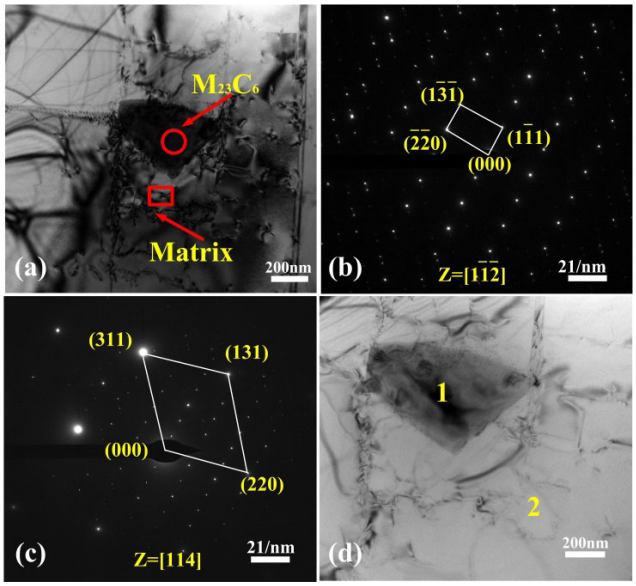

FIGURE 3. The TEM microstructure of wrought HX superalloy. (a) Selected diffraction positions in the bright-field transmission electron microscopy of M_2C_6 and the matrix; (b) and (c) SADP results of $M_{23}C_6$ and γ matrix phase; (d) EDS of area 1 and 2 in the bright-field transmission electron microscopy.

and reached a stable value (about −0.31V) (Fig. 4b). This indicates that a passivation film formed during immersion in the 10 wt.% $NaNO_3$ solution. This film formation can be explained by the fact that NO_3^- ions have stronger oxidation resistance than Cl^- ions, which promotes the formation of dense passivating immersion in the 10 wt.% $NaNO_3$ solution film [36] on the matrix surface in the 10 wt.% $NaNO_3$ solution.

The polarization curves of wrought HX tested in $NaNO_3$ and NaCl solutions are shown in Fig. 5. A stable and smooth passive zone formed in the two electrolytes with a relatively low current density (10^{-5}∼10^{-4} A/cm^2), indicating the passivation film was compact and unbroken. The passivation film's broken-down potential (E_b) in the $NaNO_3$ solution was 0.89 V_{SCE}, which was higher than the value of 0.73 V_{SCE} in NaCl solution. This difference was attributed to the high affinity and low atomic radius for chloride ions. Also, the NO_3^- ions exhibited a stronger oxidation resistance than Cl^- ions which led to a denser passivation film in $NaNO_3$ solution and further improved the E_b of the passivation film. In the transpassive region of the $NaNO_3$ solution, electrochemical dissolution and oxygen evolution took place on the surface of the anode with increasing current density because the passivation film was broken and peeled off from the matrix when the anodic potential exceeded the E_b. Neutral $NaNO_3$ solution has been widely used in the field of electrochemical processing due to its passivation characteristics, leading to improvements in machining accuracy. Interestingly, Béjar and Eterovich performed a wire-electrochemical cutting of mild steel using different solutions and found that $NaNO_3$ achieved superior cutting accuracy over NaCl [37]. It may be concluded that an accurate electrochemical dissolution process is achievable by using the $NaNO_3$ solution.

The electrolyte concentration can account for the dissolution behavior. The polarization curve of wrought HX in $NaNO_3$ solution with different concentrations at 35 °C is presented in Fig. 6a. The experimental measurement ranged

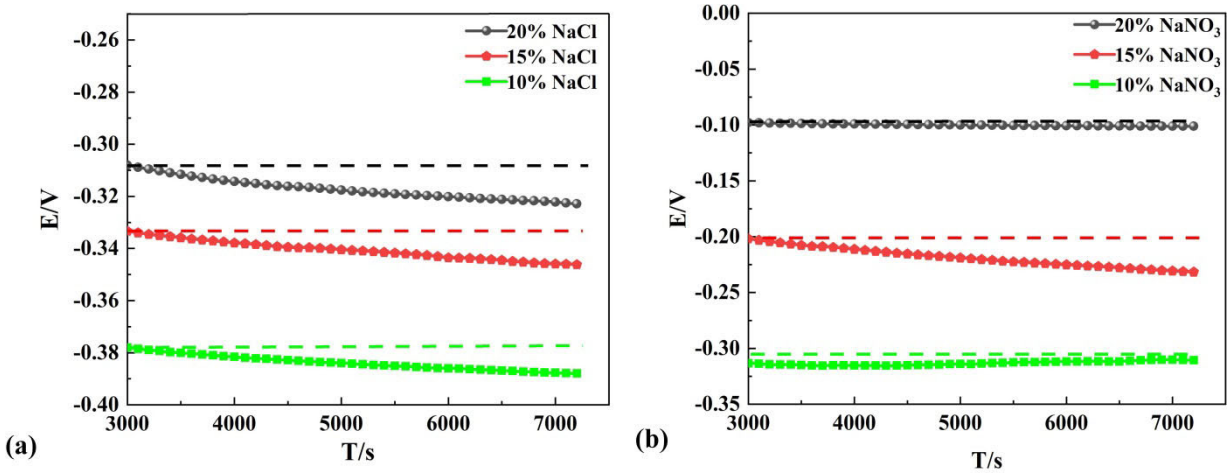

FIGURE 4. Time dependence of the E_{OCP} of wrought HX in different concentrations: (a) NaCl solution; (b) $NaNO_3$ solution.

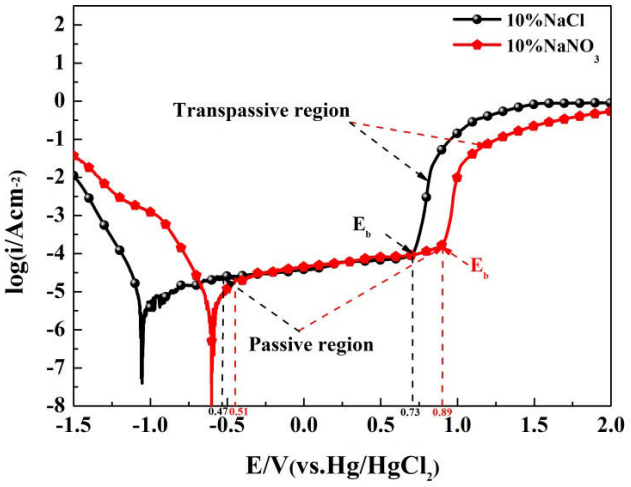

FIGURE 5. Anodic polarization curves of wrought HX in $NaNO_3$ and NaCl solutions.

from −1 to 2.7V. Electrochemical tests were performed using seven solutions with different concentrations (0.5%, 1%, 5%, 7%, 10%, 15%, and 20%). The current density clearly appeared to increase with increasing electrolyte concentrations. At lower concentrations (0.5% and 1%), it is worth noting that the current density growth rate was virtually zero. This indicates that the formation of high impedance and dense passivation film further hindered the increasing current density. The rate of change in current density increased gradually with increasing concentration (5%). The current density increased sharply when the concentration exceeded 10%. One explanation is that the conductivity and ion exchange rate at the reaction interface accelerated at higher concentrations. Therefore, it can be inferred that an efficient and stable removal rate of the material might be obtained using electrolyte concentrations of at least wt.10%, as indicated in Fig. 6a.

The effect of temperature on electrochemical dissolution is another primary factor. Fig. 6b shows that the polarization curve of wrought HX in 10wt.% $NaNO_3$ solution with different temperatures. At high temperatures (35 °C, 45 °C, 55 °C) in the transpassive region, the growth rate in current density increased sharply with increasing temperature. One possible explanation is that the higher electrolyte temperature resulted in a higher percentage of activation molecules on the reaction interface and further accelerated the intermolecular exchange rate. Therefore, employing a temperature above 35 °C can achieve stable dissolution of the material.

Based on these results, it 10wt.% $NaNO_3$ electrolyte (35 °C) could contribute to achieving wrought HX stable electrochemical dissolution.

C. CORROSION CHARACTERIZATION AND SURFACE CORROSION PRODUCTS ANALYSIS

1) CORROSION CHARACTERIZATION

The Fig. 7 shows the microstructure of wrought HX in $NaNO_3$ solution before electrochemical dissolution, at the end of passivation, transpassive dissolution, and corrosion layer expansion stage, which further illustrates the dissolution characteristics of wrought HX in 10wt.% $NaNO_3$ solution at 35 °C. The termination potential was set at 2.7 V. Fig. 7a demonstrates that an air-formed film formed on the matrix. Before achieving the E_b, a compact passivation film (about at 0.89V in Fig. 5) formed to hinder electrochemical dissolution reaction in passivation region, which was accompanied by the precipitation of $M_{23}C_6$ carbides (marked by the rectangle) at the end of passivation in Fig. 7b. Moreover, when passivation was terminated (at about 0.89 V in Fig. 5), selective local corrosion initiation of passivation film preferentially occurred along the grain boundaries or in the grain where $M_{23}C_6$ carbides were abundant, as shown in Fig. 7c. This was attributed to the defect structure of the passivation film, which forced nitrate ions from the solution into the film and

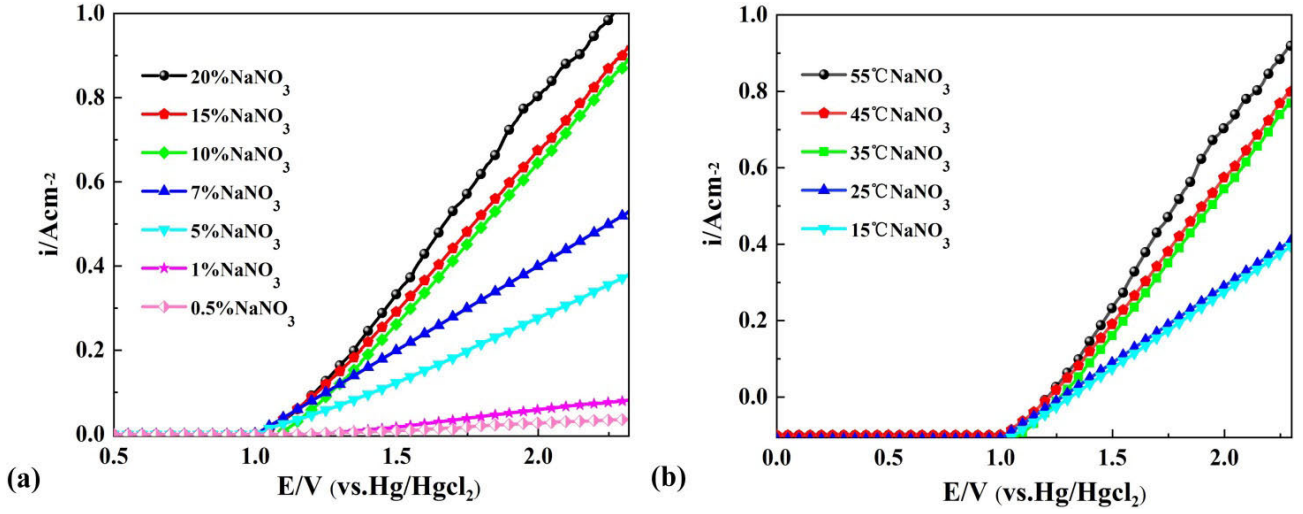

FIGURE 6. Anodic polarization curves of wrought HX in $NaNO_3$ solution. (a) different concentrations; (b) different temperatures.

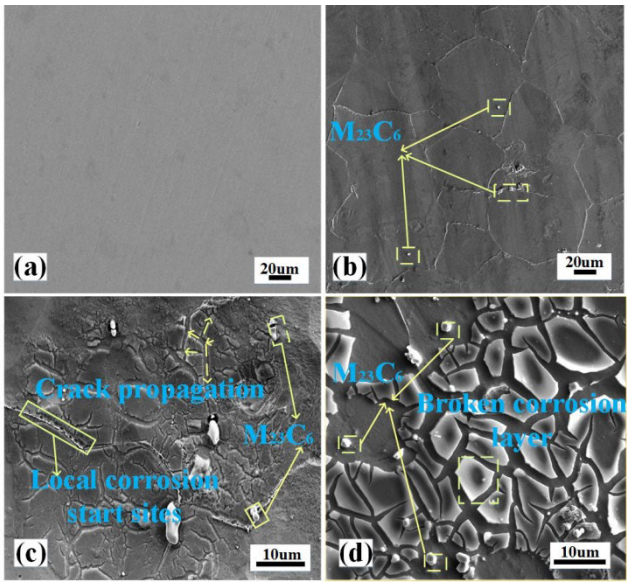

FIGURE 7. Microstructure of wrought HX at different dissolution stages. (a) before electrochemical dissolution; (b) at the end of passivation; (c) transpassive dissolution stage; (d) corrosion layer expansion.

react with cations [38]. This was mainly due to the surface integrity of the passivation film being further damaged by the chelation effect of the anions and cations [39], [40]. During the metal dissolution process in the transpassive region, the oxygen evolution reaction proceeded in parallel. As the anodic potential increased, the preferential local corrosion region of passivation film gradually expanded and microcrack propagation began to occur in the grain or at the grain boundary. At the end of crack propagation (at about 1.5 V in Fig. 5), Fig. 7d clearly indicates that the average width of the corrosion layer cracks was about 2 μm.

The EPMA analysis further determined surface products of wrought HX before and after electrochemical testing. Fig. 8a presents micro-morphology of before the electrochemical etching; Also, Cr and Mo elements were found to be uniformly distributed on the surface of matrix or enriched on the surface of gray particles, as indicated in Fig. 8b. Micro-morphology of the corrosion crack propagation is shown in Fig. 8c, and the surface microcracks were interdigitate with each other, which divided the corrosion layers into individual island-like regions. It should be noted that the local corrosion on the HX matrix preferentially occurred near the $M_{23}C_6$ or on the boundary. Finally, the corrosion pits evolved into microcracks. In addition, the effect of micro-corrosion galvanic cells between the molybdenum-rich and molybdenum-depleted regions resulted in the microcracks gradually expanding along the depth (Fig. 8d). As can be seen in Fig. 8d, the content of Ni and Fe in the region of the crack were not found to significantly decrease. Ni, Fe, and Cr were also severely depleted in the island region, which indicated that the corrosion continued to expand along the width direction. Subsequently, the width of the microcracks continued to expand with shrinking islands, and eventually the islands disappeared completely. The complete disappearance of the island-like regions is depicted in Fig. 8e. It is worth noting that the rich oxygen on the $M_{23}C_6$ is presented in Figs 8d-f. One possible explanation is that residual electrolytic products (Cr-enriched and Mo-enriched) attached to $M_{23}C_6$ particle surface.

2) SURFACE CORROSION PRODUCTS ANALYSIS

Microstructure characterization of wrought HX cross sections after solution annealing revealed the typical Fig. 9a further reveals the quantitative XPS full spectrum analysis of wrought HX before and after electrochemical testing. The surface elemental contents of Ni, Fe, and Cr were dramatically reduced and disappeared, suggesting that they were converted into metal ions, hydroxides. Nevertheless, the content of oxygen in the surface products significantly increased compared to the matrix, indicating that a large number of broken passive films formed in the surface corrosion products. As indicated in Figs. 9b_1-b_2, the compounds of the element chromium on the matrix and products were mainly presented as Cr and Cr_2O_3, respectively. The related binding energies of the Cr and Cr_2O_3 acquired from the XPS analysis were found to be 573.8 and 576.6 eV, as shown in Table II. This indicated that the electronic structure of Cr slightly changed after electrochemical dissolution, and the content of Cr in surface products was also found to be significantly reduced, as indicated in Fig. 9a. This suggested that a number of Cr compounds attaching to $M_{23}C_6$ carbides fell into the electrolyte, while residual passivation film (Cr_2O_3) remained in the surface corrosion products. Compared with Cr, the binding energy of Ni and Mo elements changed significantly, as shown in Table II, further confirming the presence of other components (e.g., NiO and MoO_3) in the residual surface corrosion products. Therefore, it is possible to conclude that the composition of broken passivation film compounds (NiO, Cr_2O_3, MoO_3) and $M_{23}C_6$ particles primarily remained on the surface of block-shape corrosion layers.

D. ELECTROCHEMICAL DISSOLUTION MECHANISM

Based on our experimental analysis, an established model was used to qualitatively depict the electrochemical dissolution characteristics of HX in $NaNO_3$ solution. The basic principle of anodic HX electrochemical dissolution using 10 wt.% $NaNO_3$ solution at 35 °C is depicted in Fig. 10. As shown in Fig. 10a, the surface of HX was assumed to be covered by a thin air-oxide film in the beginning [41],

Due to the strong oxidation of NO_3^- ions in 10 wt.% $NaNO_3$ solution, a passivation film (NiO or Cr_2O_3) was formed on the wrought HX surface [42], as shown in Fig. 10b. The matrix was covered by the passivation film, further slowing the rate of ion exchange into the matrix [43]. This is consistent with the findings of an apparent passive region of the polarization curve in Fig. 5. Preferential dissolution of M (Ni, Cr) occurred and released M^+ ions into solution. The following anodic and cathodic reactions may be expressed as equations (1) and (2), respectively. The reactions for the passivation film (M-oxides) formation on the surface

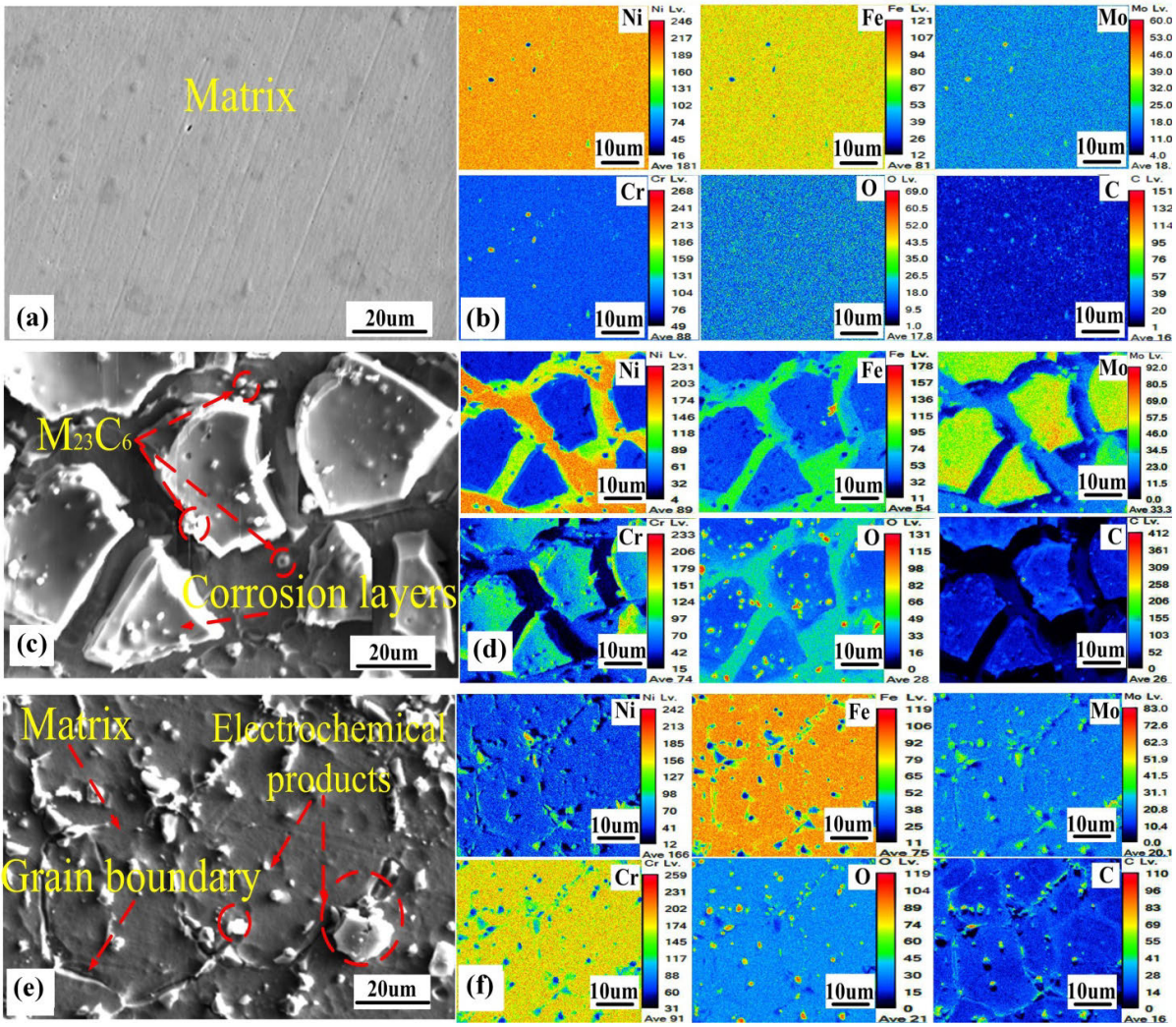

FIGURE 8. EPMA results of wrought HX before and after electrochemical testing. (a), (c), and (e) show BSE morphology; (b), (d), and (f) show the element distribution of wrought HX.

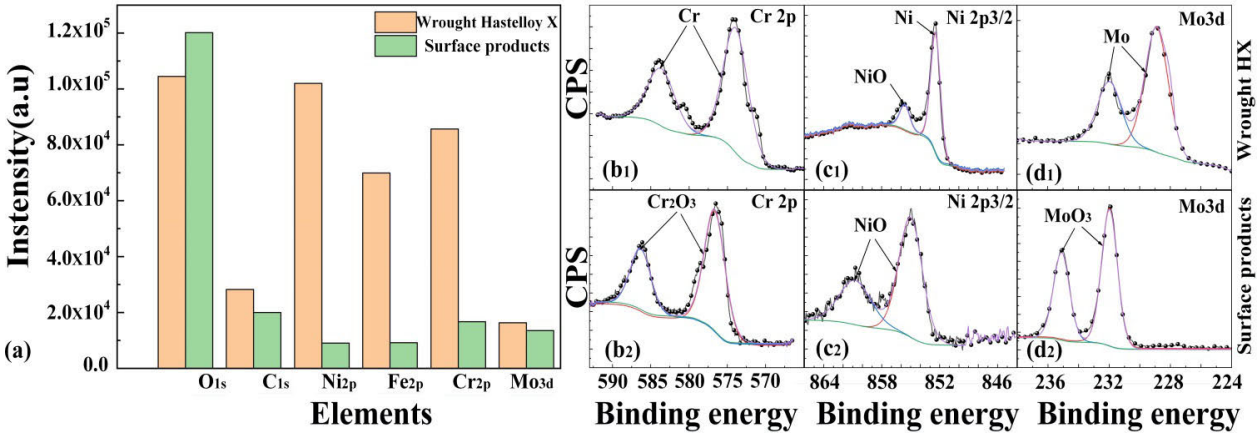

FIGURE 9. XPS spectra of wrought HX and matrix surface products after Ar ion cleaning. (a) Quantitative XPS full spectrum analysis after Ar ion cleaning. (a) Quantitative XPS full spectrum analysis results; (b) Cr 2p; (c) Mo 2p3/2; (d) Mo 3d.

and the final productions can be expressed as equations (3) and (4):

$$M \rightarrow M^+ + e^- \quad (1)$$

$$2H_2O + O_2 + 4e^- + \rightarrow 4OH^- \quad (2)$$

$$M^+ + OH^- \rightarrow M\,OH \quad (3)$$

$$M\,OH + OH^- \rightarrow MO + H_2O \quad (4)$$

At the end of the passivation stage (Fig. 10c), a large number of NO_3^- ions started to accumulate above the surface of

TABLE 2. Binding energies and compounds of wrought hx and surface products acquired from xps analysis.

Element	Compounds	Binding energies on matrix	Binding energies on surface products
Cr	Cr_{met}	573.8	–
	Cr_2O_3	–	576.6
Ni	Ni_{met}	852.4	–
	NiO	–	855.0
Mo	Mo_{met}	228.0	–
	MoO_3	–	232.5

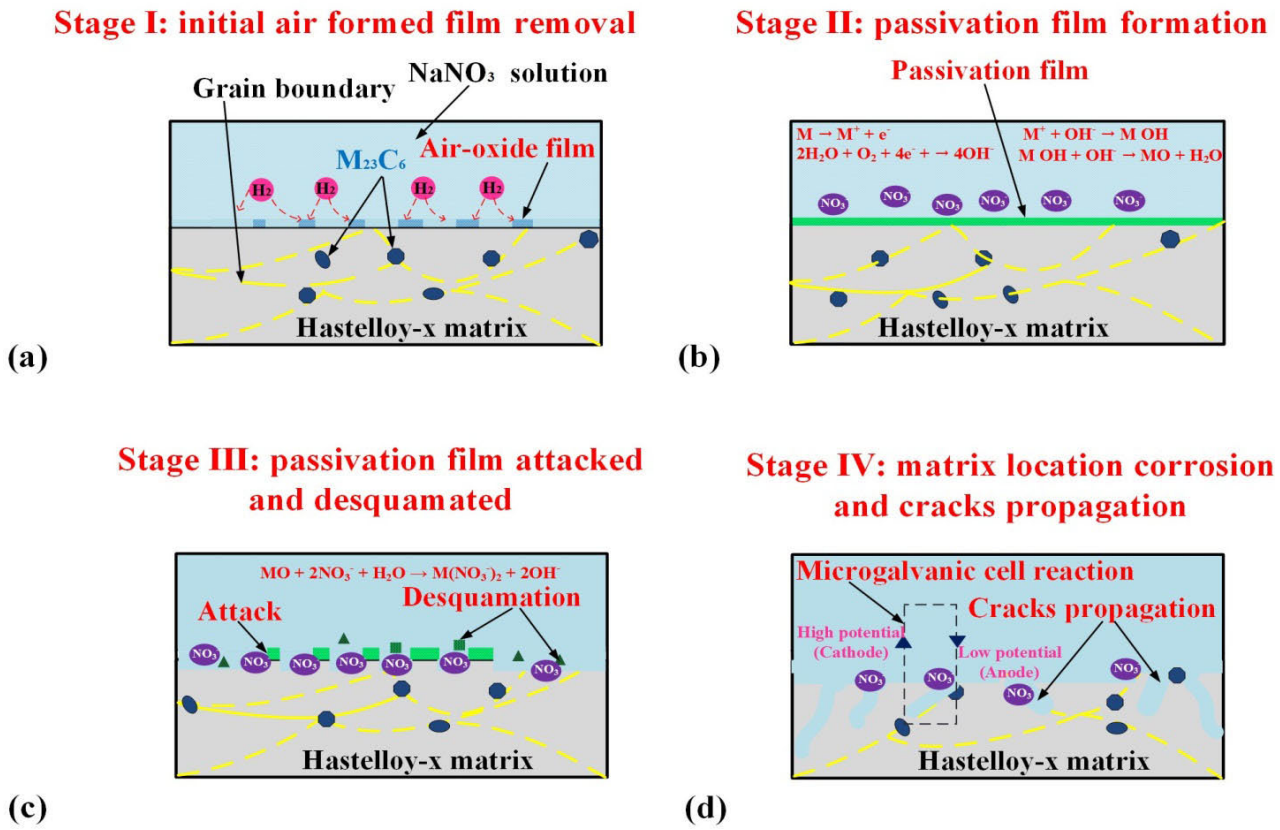

FIGURE 10. Schematic of the electrochemical dissolution behavior of HX in $NaNO_3$ solution. (a) Stage I: initial air formed film removal; (b) Stage II: passivation film formation; (c) Stage III: passivation film attacked and desquamated; (d) Stage IV: matrix location corrosion and crack propagation.

the passivation film. The NO_3^- ions then gradually diffused into the film/solution interface from the electrolyte solution with increasing potential, resulting in the heavy attack of the passivation film. Furthermore, local corrosion near the grain boundary (Fig. 7c) also occurred, which contributed to the electrolyte solution penetrating into the crevice at the film/matrix interface. When the repair rate of the passivation film was less than its active dissolution rate, the local corrosion region of passivation film gradually expanded and began to peel. Over time, the local corrosion propagation effect also contributed to further fragmentation of the oxide layer and its separation from the matrix, resulting in the complete exposure of the matrix and the expansion of the dissolution area. This further accelerated the corrosion rate of the matrix with increasing density of the corrosion current. The primary reaction in this stage may be expressed as equation (5):

$$MO + 2NO_3^- + H_2O \rightarrow M(NO_3^-)_2 + 2OH^- \quad (5)$$

The passivation film layers were completely dissolved and removed as current density increased, which led to the matrix being exposed to the electrolyte, as indicated in Fig. 10d. In addition, a large number of discontinuous $M_{23}C_6$ particles were exposed on the grain boundary of matrix region after the passivation film was etched. This was consistent with the exposure of Mo_2C, Cr_7C_3 and Al_4C_3 carbides in the dissolution process of stainless steel in molten FLiBe salt by Zheng *et al.* [44]. For $M_{23}C_6$ particles, a large number of Cr elements were enriched on their surface due to the segregation of Cr element (Fig. 8d), which led to a decrease in the distribution of Cr elements and further accelerated local

corrosion in the area around $M_{23}C_6$ particles. On the one hand, selective corrosion around the carbides was preferentially caused by the fact that between $M_{23}C_6$ particles and matrix forms numerous tiny galvanic cells. On the other hand, as an induced corrosion defect, $M_{23}C_6$ particles may provide a fast diffusion path for Cr and Mo elements on the grain boundary, which resulted in element segregation and further acceleration of the expansion in local corrosion areas. The microcrack growth around the $M_{23}C_6$ particles is depicted in Fig. 7c.

In this acceleration stage of microcephalic cell corrosion (Fig. 10d), the local corrosion propagation in the $M_{23}C_6/\gamma$ interface near the grain boundary can occur below the pitting potential, which may result in the propagation of the local corrosion. Therefore, when local corrosion pits nucleate at the site, it could accelerate micro-galvanic corrosion and enlarge the depth of corrosion pits. Eventually, cracks in the corrosion layer widened and gradually peeled off, exposing the new matrix. In addition, the Ni, Fe, and Cr elements in the matrix region are converted to Fe^{3+}, Ni^{2+} and $HCrO_4^-$ during the electrochemical dissolution process, as reported by M. A. Cavanaugh [45].

IV. CONCLUSION

This study investigated the electrochemical dissolution behavior of wrought HX, and various electrochemical measurement factors of this setup were investigated, including electrolytes type, anodic polarization curves, and open-circuit potentials. In particular, the microstructure characteristics were systematically examined in the present study. This study also highlighted the correlation between the carbides precipitates and the electrochemical dissolution behavior of wrought HX. The conclusions of this study may be summarized as follows:

(1) The microstructure analysis revealed that fine equiaxed crystals with strong random texture were formed in the wrought HX; the precipitate phase in wrought alloy HX was carbide, which was mainly distributed on the grain boundaries or within the grains. The SADP and EDS results confirmed that the gray particles were the Cr-enriched and Mo-enriched $M_{23}C_6$ type precipitates.

(2) Quantified comparison results between the open-circuit potentials and the anodic polarization curves confirmed that they were more stable in $NaNO_3$ solution than in NaCl solution during the electrochemical dissolution process for wrought HX. An appropriate temperature (35 °C) and concentration (10%) contributed to achieving an efficient dissolution process in $NaNO_3$ solution.

(3) EPMA showed that the residual passivation film compounds were examined to easily adhere to the corrosion layers surface, especially the areas enriched $M_{23}C_6$ particles. XPS results demonstrated that the surface corrosion products were mixtures of NiO, Cr_2O_3, and MoO_3.

(4) The selective dissolution of the wrought HX matrix was achieved because both the segregation on the grain boundaries and the presence of $M_{23}C_6$ carbides in the grain boundaries could contribute to the formation of a number of preferred sites for corrosion galvanic cells between $M_{23}C_6$ and the γ matrix, resulting in the formation of micro-corrosion cracks.

REFERENCES

[1] A. R. Mount, P. S. Howarth, and D. Clifton, "The use of a segmented tool for the analysis of electrochemical machining," *J. App. Electrochem.*, vol. 31, no. 11, pp. 1213–1220, Nov. 2001.

[2] Z. Zhu, D. Wang, J. Bao, N. Wang, and D. Zhu, "Cathode design and experimental study on the rotate-print electrochemical machining of revolving parts," *Int. J. Adv. Manuf. Technol.*, vol. 80, nos. 9–12, pp. 1957–1963, Oct. 2015.

[3] D. Zhan, L. Han, J. Zhang, K. Shi, J.-Z. Zhou, Z.-W. Tian, and Z.-Q. Tian, "Confined chemical etching for electrochemical machining with nanoscale accuracy," *Accounts Chem. Res.*, vol. 49, no. 11, pp. 2596–2604, Nov. 2016.

[4] D. Zhan, L. Han, J. Zhang, Q. He, Z.-W. Tian, and Z.-Q. Tian, "Electrochemical micro/nano-machining: Principles and practices," *Chem. Soc. Rev.*, vol. 46, no. 5, pp. 1526–1544, Feb. 2017.

[5] L. Meng, Y. Zeng, and D. Zhu, "Investigation on wire electrochemical micro machining of Ni-based metallic glass," *Electrochimica Acta*, vol. 233, pp. 274–283, Apr. 2017.

[6] M. Bassu, S. Surdo, L. M. Strambini, and G. Barillaro, "Electrochemical micromachining as an enabling technology for advanced silicon microstructuring," *Adv. Funct. Mater.*, vol. 22, no. 6, pp. 1222–1228, Mar. 2012.

[7] K. Kim, B. Ki, K. Choi, and J. Oh, "Anodic imprint lithography: Direct imprinting of single crystalline GaAs with anodic stamp," *ACS Nano*, vol. 13, no. 11, pp. 13465–13473, Nov. 2019.

[8] M.-R. Zhang, Q.-M. Jiang, S.-H. Zhang, Z.-G. Wang, F. Hou, and G.-B. Pan, "Fabrication of gallium nitride nanowires by metal-assisted photochemical etching," *Appl. Surf. Sci.*, vol. 422, pp. 216–220, Nov. 2017.

[9] F. Carpignano, S. Surdo, G. Barillaro, and S. Merlo, "Silicon micromachined device testing by infrared low-coherence reflectometry," *J. Microelectromech. Syst.*, vol. 24, no. 6, pp. 1960–1964, Dec. 2015.

[10] S. Surdo, F. Carpignano, G. Silva, S. Merlo, and G. Barillaro, "An all-silicon optical platform based on linear array of vertical high-aspect-ratio silicon/air photonic crystals," *Appl. Phys. Lett.*, vol. 103, no. 17, Oct. 2013, Art. no. 171103.

[11] K. P. Rajurkar, D. Zhu, J. A. McGeough, J. Kozak, and A. De Silva, "New developments in electro-chemical machining," *CIRP Ann.*, vol. 48, no. 2, pp. 567–579, 1999.

[12] D. Zhu and H. Y. Xu, "Improvement of electrochemical machining accuracy by using dual pole tool," *J. Mater. Process. Technol.*, vol. 129, nos. 1–3, pp. 15–18, Oct. 2002.

[13] A. K. M. De Silva, H. S. J. Altena, and J. A. McGeough, "Influence of electrolyte concentration on copying accuracy of precision-ECM," *CIRP Ann.*, vol. 52, no. 1, pp. 165–168, Jun. 2004.

[14] J. Bannard, "Effect of flow on the dissolution efficiency of mild steel during ECM," *J. Appl. Electrochem.*, vol. 7, no. 3, pp. 267–270, May 1977.

[15] L. Tang, B. Li, S. Yang, Q. Duan, and B. Kang, "The effect of electrolyte current density on the electrochemical machining S-03 material," *Int. J. Adv. Manuf. Technol.*, vol. 71, nos. 9–12, pp. 1825–1833, Apr. 2014.

[16] N. S. Qu, X. L. Fang, Y. D. Zhang, and D. Zhu, "Enhancement of surface roughness in electrochemical machining of Ti6Al4 V by pulsating electrolyte," *Int. J. Adv. Manuf. Technol.*, vol. 69, nos. 9–12, pp. 2703–2709, Dec. 2013.

[17] B. Bhattacharyya, M. Malapati, J. Munda, and A. Sarkar, "Influence of tool vibration on machining performance in electrochemical micro-machining of copper," *Int. J. Mach. Tools Manuf.*, vol. 43, no. 13, pp. 1301–1310, Oct. 2003.

[18] B. Bhattacharyya, J. Munda, and M. Malapati, "Advancement in electrochemical micro-machining," *Int. J. Mach. Tools Manuf.*, vol. 44, no. 15, pp. 1577–1589, Dec. 2004.

[19] X. Wang, N. Qu, X. Fang, and H. Li, "Electrochemical drilling with constant electrolyte flow," *J. Mater. Process. Technol.*, vol. 238, pp. 1–7, Dec. 2016.

[20] X. Fang, N. Qu, Y. Zhang, Z. Xu, and D. Zhu, "Improvement of hole exit accuracy in electrochemical drilling by applying a potential difference between an auxiliary electrode and the anode," *J. Mater. Process. Technol.*, vol. 214, no. 3, pp. 556–564, Mar. 2014.
[21] J. Wang, Y. Zhang, and Y. Yu, "Recent advances of PECM (pulse ECM) in the precision/micro machining areas," *China Mech. Eng.*, vol. 18, no. 1, pp. 114–119, Jan. 2007.
[22] N. Dai, L.-C. Zhang, J. Zhang, X. Zhang, Q. Ni, Y. Chen, M. Wu, and C. Yang, "Distinction in corrosion resistance of selective laser melted Ti-6Al-4 V alloy on different planes," *Corrosion Sci.*, vol. 111, pp. 703–710, Oct. 2016.
[23] G.-L. Song, R. Mishra, and Z. Xu, "Crystallographic orientation and electrochemical activity of AZ31 Mg alloy," *Electrochem. Commun.*, vol. 12, no. 8, pp. 1009–1012, Aug. 2010.
[24] N. Dai, L.-C. Zhang, J. Zhang, Q. Chen, and M. Wu, "Corrosion behavior of selective laser melted Ti-6Al-4 V alloy in NaCl solution," *Corrosion Sci.*, vol. 102, pp. 484–489, Jan. 2016.
[25] L. Kops and V. B. Quach, "Investigation on the role of workpiece grain size in electrochemical machining process," *J. Eng. Ind.*, vol. 98, no. 1, pp. 360–368, Feb. 1976.
[26] D. Landolt, R. H. Muller, and C. W. Tobias, "Crystallographic factors in high-rate anodic dissolution of copper," *J. Electrochemical Soc.*, vol. 118, no. 1, pp. 36–40, Jan. 1971.
[27] P. Guo, X. Lin, J. Xu, J. Li, J. Liu, and W. Huang, "Electrochemical removal of different phases from laser solid formed inconel 718," *J. Electrochem. Soc.*, vol. 164, no. 7, pp. E151–E157, May 2017.
[28] P. Guo, X. Lin, and W. Huang, "Columnar structure and electrochemical anisotropy of a nickel-based superalloy fabricated via laser solid forming," *J. Appl. Electrochem.*, vol. 47, no. 9, pp. 1083–1090, Sep. 2017.
[29] K. Han, V. Toplosky, N. Min, J. Lu, Y. Xin, and R. Walsh, "High modulus reinforcement alloys," *IEEE Trans. Appl. Supercond.*, vol. 28, no. 3, pp. 1–5, Apr. 2018.
[30] Q. Han, Y. Gu, R. Setchi, F. Lacan, R. Johnston, S. L. Evans, and S. Yang, "Additive manufacturing of high-strength crack-free Ni-based hastelloy X superalloy," *Additive Manuf.*, vol. 30, Dec. 2019, Art. no. 100919.
[31] S. Kinzel, J. Gabel, R. Völkl, and U. Glatzel, "Reasons for volume contraction after long-term annealing of waspaloy," *Adv. Eng. Mater.*, vol. 17, no. 8, pp. 1106–1112, Aug. 2015.
[32] X. Xiang, Z. Yao, J. Dong, and L. Sun, "Dissolution behavior of intragranular M23C6 carbide in 617B Ni-base superalloy during long-term aging," *J. Alloys Compounds*, vol. 787, pp. 216–228, May 2019.
[33] M. Terada, M. Saiki, I. Costa, and A. F. Padilha, "Microstructure and intergranular corrosion of the austenitic stainless steel 1.4970," *J. Nucl. Mater.*, vol. 358, no. 1, pp. 40–46, Nov. 2006.
[34] G. Marchese, G. Basile, E. Bassini, A. Aversa, M. Lombardi, D. Ugues, P. Fino, and S. Biamino, "Study of the microstructure and cracking mechanisms of hastelloy X produced by laser powder bed fusion," *Materials*, vol. 11, no. 1, p. 106, Jan. 2018.
[35] G. Marchese, E. Bassini, A. Aversa, M. Lombardi, D. Ugues, P. Fino, and S. Biamino, "Microstructural evolution of post-processed hastelloy X alloy fabricated by laser powder bed fusion," *Materials*, vol. 12, no. 3, p. 486, Feb. 2019.
[36] T. Tzvetkoff, "Mechanism of formation of corrosion layers on nickel and nickel-based alloys in melts containing oxyanions—A review," *Mater. Chem. Phys.*, pp. 897–904, Sep. 2003.
[37] P. S. Pa, "Super finishing with ultrasonic and magnetic assistance in electrochemical micro-machining," *Electrochimica Acta*, vol. 54, no. 25, pp. 6022–6027, Oct. 2009.
[38] T. P. Hoar, "The production and breakdown of the passivity of metals," *Corrosion Sci.*, vol. 7, no. 6, pp. 341–355, Nov. 2004.
[39] J. Galvele, "Transport processes in passivity breakdown—II. Full hydrolysis of the metal ions," *Corrosion Sci.*, vol. 21, no. 8, pp. 551–579, May 2003.
[40] I. Katsounaros, D. Ipsakis, C. Polatides, and G. Kyriacou, "Efficient electrochemical reduction of nitrate to nitrogen on tin cathode at very high cathodic potentials," *Electrochimica Acta*, vol. 52, no. 3, pp. 1329–1338, Nov. 2006.
[41] M. Datta, "AES/XPS study of transpassive films on iron in nitrate solution," *J. Electrochem. Soc.*, vol. 131, no. 11, pp. 2484–2489, Nov. 1984.
[42] B. B. Rodriguez and A. W. Hassel, "Passivity of a nanostructured directionally solidified NiAl–Re alloy as substrate for electrodeposition of gold," *J. Electrochem. Soc.*, vol. 155, no. 3, pp. K31–K37, Jan. 2008.
[43] E. Saebnoori, T. Shahrabi, H. Jafarian, and M. Ghaffari, "Changes in the resistance to corrosion of thermally passivated titanium aluminide during exposure to sodium chloride solution," *Res. Chem. Intermediates*, vol. 41, no. 2, pp. 1079–1095, Feb. 2015.
[44] G. Zheng, L. He, D. Carpenter, and K. Sridharan, "Corrosion-induced microstructural developments in 316 stainless steel during exposure to molten Li_2BeF_4(FLiBe) salt," *J. Nucl. Mater.*, vol. 482, pp. 147–155, Dec. 2016.
[45] M. A. Cavanaugh, J. A. Kargol, J. Nickerson, and N. F. Fiore, "The anodic dissolution of a Ni-base superalloy," *CORROSION*, vol. 39, no. 4, pp. 144–150, Apr. 1983.

YINGYUE YIN received the M.S. degree in mechanical engineering from Xinjiang University, Urumqi, China, in 2017. He is currently pursuing the Ph.D. degree in mechanical engineering with the School of Mechanical Engineering, Shandong University, Jinan, China.

His research interests include basic research on the dissolution mechanism and electrochemical processing technology of Hastelloy X alloy.

JIANHUA ZHANG received the M.S. and Ph.D. degrees in mechanical engineering from Shandong University, Jinan, China, in 1991.

He was a Professor, in 1995, and a Doctoral Supervisor, in 1997. From April 2000 to October 2000, he went to The Hong Kong Polytechnic University for collaborative scientific research. From December 2006 to November 2007, he went to Carnegie Mellon University for visiting scholar research. His research interests include high-efficiency precision composite processing technology and numerical control equipment research.

YUCAI MA received the B.S. degree in mechanical engineering from the Shandong University of Technology, Zibo, China, in 2019. He is currently pursuing the master's degree in mechanical engineering with the School of Mechanical Engineering, Shandong University, Jinan, China.

His research interest includes the principle of special processing and its application.

JINXING HUO received the B.S. degree in mechanical engineering from Shandong University, Jinan, China, in 2018, where he is currently pursuing the M.S. degree in mechanical engineering with the School of Mechanical Engineering.

His research interest includes the processing on difficult-to-cut materials and its application.

KAI ZHAO received the M.S. degree in material science and technology from Northwestern Polytechnical University, Xi'an, China, in 2015. He is currently pursuing the Ph.D. degree in material science and technology with Shandong University, Jinan, China.

His research interest includes the processing of 7xxx Al alloys and its application.

XIANGYU MENG received the B.S. degree in mechanical engineering from Shandong Jiaotong University, Jinan, China, in 2017. He is currently pursuing the M.S. degree in mechanical engineering with the School of Mechanical Engineering, Shandong University, Jinan, China.

His research interest includes the non-traditional processing on difficult-to-cut materials and its application.

QUANQUAN HAN received the B.Sc. degree from Shandong University, China, in 2014, and the Ph.D. degree from Cardiff University, U.K., in 2017.

From August 2017 to April 2019, he was a Research Associate with the School of Engineering, Cardiff University. He is currently a Full Professor in additive manufacturing with the School of Mechanical Engineering, Shandong University, China. He has published more than 15 peer reviewed articles in additive manufacturing. He was a recipient of the David Douglas Award, in 2017 from the South Wales Institute of Engineers Educational Trust.

JICAI YIN received the B.S., M.S., and Ph.D. degrees, in 2008, 2011, and 2016, respectively.

His research interests include advanced manufacturing technology and equipment, and advanced engineering materials.